MNRAS **000**, 1–11 (2018) Preprint 14 September 2018 Compiled using MNRAS LATEX style file v3.0

Predictions for the spatial extent of the dust continuum emission in $2 < z < 5$ star-forming galaxies

R. K. Cochrane, [1,2]★ C. C. Hayward,[3] D. Anglés-Alcázar,[3] J. Lotz,[4] T. Parsotan[5]
[1] *SUPA, Institute for Astronomy, Royal Observatory Edinburgh, EH9 3HJ, UK*
[2] *Isaac Newton Group of Telescopes, E-38700 Santa Cruz de La Palma, Canary Islands, Spain*
[3] *Center for Computational Astrophysics, Flatiron Institute, 162 Fifth Avenue, New York, NY 10010, USA*
[4] *Space Telescope Science Institute, 3700 San Martin Drive, Baltimore, MD 21218, USA*
[5] *Department of Physics, Oregon State University, 301 Weniger Hall, Corvallis, OR 97331, U.S.A.*

14 September 2018

ABSTRACT

We present the first detailed study of the spatially-resolved dust continuum emission of simulated high-redshift galaxies. We run the SKIRT radiative transfer code on a subsample of far-infrared/submillimeter-bright snapshots of Milky Way mass, high redshift galaxies drawn from the FIRE-2 simulations. These simulations are the state-of-the-art in zoom-in cosmological hydrodynamical simulations. Our modelling provides predictions for the full rest-frame far-ultraviolet-to-far-infrared Spectral Energy Distributions of these simulated galaxies, as well as maps of their emission across the wavelength spectrum, resolved to 25pc spatial scales. The derived morphologies are notably different in different wavebands, with the same galaxy appearing clumpy and extended in the far-ultraviolet yet compact at far-infrared wavelengths. The observed-frame 870μm half-light radii of our FIRE-2 galaxies are $\sim 0.5-3$kpc, consistent with existing ALMA observations of high redshift galaxies. In both simulated and observed galaxies, the dust continuum emission is more compact than the cold gas, but more extended than the stellar component. The most extreme cases of compact dust emission seem to be driven by particularly compact recent star formation.

Key words: galaxies: evolution – galaxies: starburst – galaxies: star formation – submillimetre: galaxies – radiative transfer – infrared: galaxies

1 INTRODUCTION

Observations suggest that the physical properties of star-forming (SF) galaxies at the peak of cosmic star-formation ($z \sim 2$) differ greatly from those of the ordered disks and ellipticals in the local Universe. Galaxies at these redshifts display high star-formation rates, believed to be driven by high molecular gas fractions (Tacconi et al. 2010, 2013) that arise due to steady accretion of cold gas along filaments of the cosmic web (Dekel et al. 2009). Structurally, high redshift galaxies are less ordered than their low redshift counterparts, with star formation taking place within turbulent disks (Genzel et al. 2008; Guo et al. 2015) that often harbour massive ultraviolet (UV)-bright clumps (Elmegreen et al. 2013). However, our measurements of the high-redshift Universe are largely reliant on data at rest-frame optical and UV wavelengths.

Only in the last few years have new facilities such as ALMA had the resolving power to probe longer wavelength emission from highly star-forming galaxies. The angular resolution of previous instruments such as SCUBA was low, so it was not possible to determine the structural properties of high redshift galaxies. Source confusion has also been a hindrance in the identification of fainter sources (e.g. with Herschel; Oliver et al. 2012; Scudder et al. 2016). ALMA has the potential to be particularly fruitful in identifying high redshift galaxies, due to the so-called 'negative k-correction' (far-infrared flux from galaxies with similar intrinsic spectra remains approximately constant across the redshift range $z \sim 1-6$, as we trace further up the Rayleigh-Jeans tail). The most interesting physical insights will likely come from the combination of these new millimeter/sub-millimeter (mm/sub-mm) data with shorter-wavelength imaging. To this end, Dunlop et al. (2017) present 1.3mm ALMA imag-

★ E-mail: rcoch@roe.ac.uk

ing of the Hubble UltraDeep Field (HUDF), previously mapped with the Wide Field Camera 3/IR on the Hubble Space Telescope (HST) to an unprecedented 5σ depth of 30AB mag (Bouwens et al. 2010; Oesch et al. 2010; Illingworth et al. 2013; Dunlop et al. 2013; Ellis et al. 2013), and also with HST Advanced Camera for Surveys (ACS; Beckwith et al. 2006), over an area of 4.5arcmin^2. Combining this new ALMA data with Herschel and Spitzer-24μm photometry and fitting to a template Spectral Energy Distribution (SED), they find that $\sim$ 85% of the total star-formation at $z \sim 2$ is enshrouded in dust. For high-mass galaxies ($M_* > 2 \times 10^{10} M_\odot$), which host $\sim$ 65% of the total star-formation at this epoch, the star-formation rate derived from long-wavelength emission is an extraordinary 200 times that derived from unobscured light. Bowler et al. (2018) show that dust-obscured star-formation could be substantial even as early as $z \sim 7$.

In addition to substantially different measurements of star formation rates, studies of galaxies at longer wavelengths also present a different view of the morphologies of high-redshift galaxies. Unobscured emission (probed at short wavelengths) tends to be significantly more extended and clumpier than the rest-frame far-infrared (FIR) emission. Barro et al. (2016), for example, find that the 345GHz (ALMA Band 7) dust continuum emission of a $z = 2.45$ galaxy has a half-light radius half of that of the rest-frame optical emission probed by HST. Hodge et al. (2016) image 16 $z \sim 2.5$ luminous sub-mm galaxies at 0.16″ in the same ALMA band. Many of these galaxies display clumpy structures in HST H_{160} & I_{814} bands, but their dust emission appears substantially smoother and more compact. The 870μm radii obtained are $\sim$ 2kpc, with no convincing evidence for clumpy dust emission at the ALMA resolution probed.

Molecular gas reservoirs have also been mapped for a handful of high-redshift, FIR-luminous galaxies. High spatial resolution studies show that molecular gas is compact, though it tends to be slightly more extended than the dust continuum emission. Tadaki et al. (2017) image two $z = 2.5$ galaxies at 345GHz, obtaining 870μm-obtained dust radii of $\sim$ 1kpc, around half the size of the CO(J=3-2) emission. Consistent results have been found by other studies (e.g. Calistro Rivera et al. 2018), though sample sizes remain small.

A physical understanding of these differences in spatial extent of emission in different wavebands is critical in order to make the best use of the unmatched sensitivity and high spatial resolution of ALMA. This is currently difficult observationally, as only small samples of galaxies have been resolved at high resolution with multiple instruments, and such samples are often biased towards either the least dust-obscured systems (if selected in the UV) or the most compact, FIR-bright systems (if selected by FIR surface brightness). Interpretations are further complicated by uncertainty in what FIR/sub-mm fluxes actually probe. Frequently used linear relations between observed FIR/sub-mm flux and SFR (e.g. Kennicutt & Evans 2012) do not fold in the shape of the full dust SED, which should reflect not only SFR but also dust mass, dust temperature, and the geometry of the source (Hayward et al. 2011).

The primary aim of this paper is to understand which physical properties of high-redshift galaxies are probed by their dust continuum emission, in a spatially-resolved manner. We address this using simulations, to study individual galaxies at high spatial resolution across the rest-frame UV-FIR spectrum. We draw a sample of the most FIR-bright galaxies within The Feedback In Realistic Environments 2 (FIRE 2) simulations (Hopkins et al. 2014, 2017). We perform 3D continuum radiative transfer on selected galaxy snapshots within the simulations, modelling the effects of dust extinction across the wavelength spectrum to obtain predictions for the spatially-resolved multi-wavelength emission of these high redshift FIR/sub-mm-bright galaxies. We then compare the spatial extent of the dust continuum emission to the intrinsic physical properties of our simulated galaxies.

The structure of this paper is as follows. In Section 2, we present the selection of the snapshots within the FIRE-2 simulations at which the modelled galaxies are highly star-forming and predicted to be sub-mm-bright. We describe the sophisticated radiative transfer modelling used to post-process these galaxy snapshots and present the predictions for their rest-frame UV-FIR spectral energy distributions in Section 3. We present predictions for the spatial extent of dust continuum emission from the galaxies in Section 4, and also compare our predictions to observational results. Finally, we study which physical properties of high-redshift, highly star-forming galaxies are best probed by the spatial extent of the dust continuum emission.

2 A SAMPLE OF SIMULATED HIGH-REDSHIFT GALAXIES

2.1 Galaxies in FIRE-2

The Feedback In Realistic Environments (FIRE) project (Hopkins et al. 2014, 2017) is a set of state-of-the-art hydrodynamical cosmological zoom-in simulations that explore the role of feedback in galaxy formation and evolution. Stellar feedback must play an important role in galaxy formation. Without it, galaxies would cool on timescales shorter than their dynamical times, leading to gravitational collapse, fragmentation and accelerated star-formation. Galaxies simulated without stellar feedback thus rapidly become far more massive than observed (Hopkins et al. 2011). The tight locus of observed galaxies on the Kennicutt-Schmidt relation (Kennicutt 1998) implies that gas consumption timescales in real galaxies are long. Futhermore, both the galaxy stellar mass function (e.g. Ilbert et al. 2013; Muzzin et al. 2013) and the stellar mass-halo mass relation (see, e.g. Moster et al. 2010; Behroozi et al. 2013) imply that galaxies retain only a small fraction of the universal baryon fraction in stars. These pieces of observational evidence, together with the observed enrichment of the CGM and IGM, demand that stellar feedback must be at play.

Various stellar feedback processes are thought to contribute, being particularly important in low stellar mass galaxies, below the peak of the stellar mass - halo mass relation. These include supernovae, protostellar jets, photo-heating, stellar mass loss from O- and AGB-stars and radiation pressure (see Dale 2015, for a review). Importantly, these processes are believed to act non-linearly, and so modelling the stellar processes of even a single galaxy becomes a complex computational challenge. This

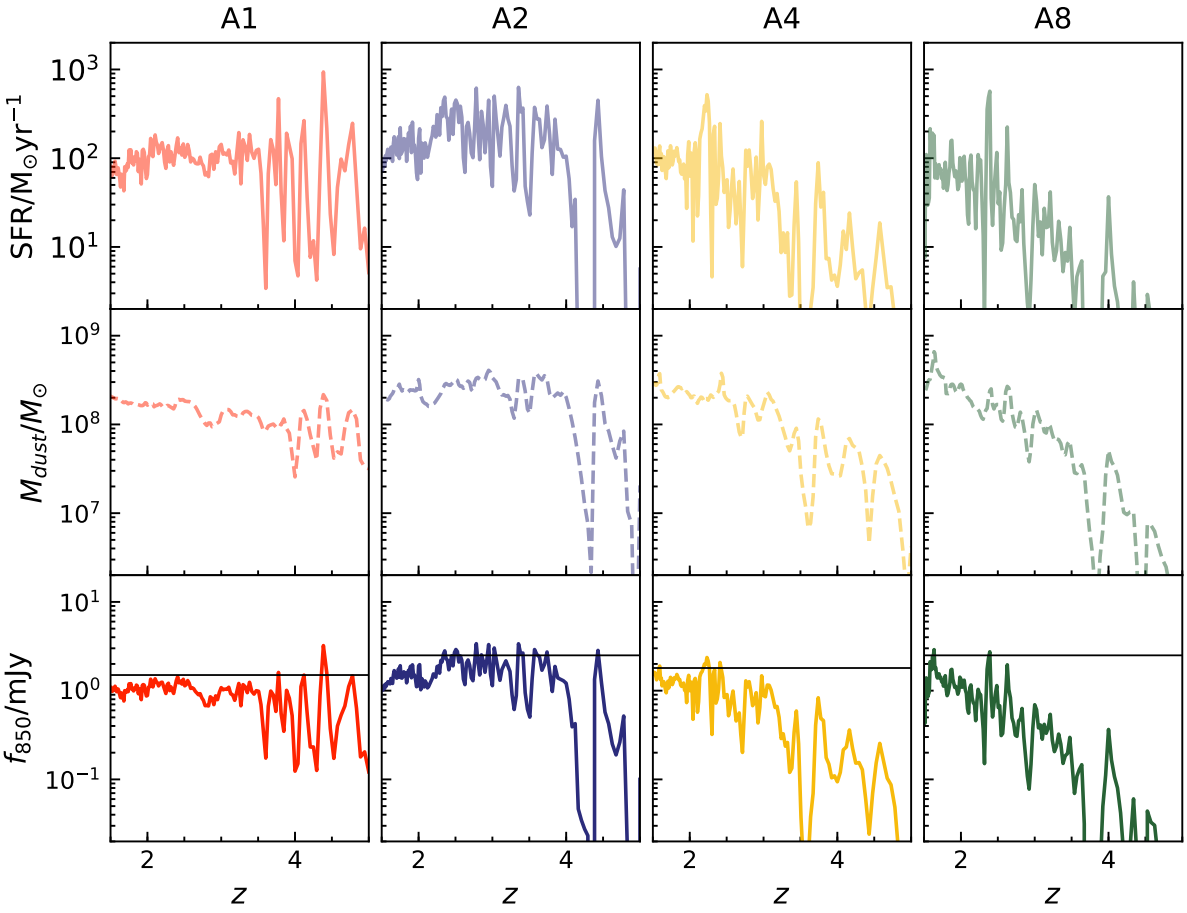

Figure 1: The evolution of star formation rate (top), dust mass (middle) and rough predicted 850μm flux (bottom) for our four simulated galaxies. We select a sample of likely sub-mm bright snapshots for each galaxy based on predicted 850μm flux, as shown by the black horizontal line on the lower panel.

has recently become possible at high resolution, with the FIRE simulations.

The FIRE project employs two main techniques to aid in creating realistic galaxies. Firstly, FIRE resolves the formation of giant molecular clouds (GMCs), which limit the rate of star formation in galactic disks. Star formation takes place in self-gravitating, self-shielding molecular gas at high densities ($n_H > 1000\mathrm{cm}^{-3}$ in the simulations we use here). Secondly, FIRE includes models for both energy and momentum return from the main stellar feedback processes, using the predictions of stellar population synthesis models without extensive parameter tuning. Overall, this project represents substantial progress over older simulations, which relied much more heavily on sub-grid models, limiting their predictive power. The most recent FIRE simulations succeed in broadly reproducing observed galaxy properties, including stellar masses, star-formation histories and the 'main sequence' of star-forming galaxies (see Hopkins et al. 2014; Sparre et al. 2017), metallicities and abundance ratios (Ma et al. 2016; van de Voort et al. 2015), as well as morphologies and kinematics of both thin and thick disks (Ma et al. 2016).

For this paper we choose a subsample of four simulated galaxies that reach Milky Way masses by $z = 2$. The halos selected cover a range of halo formation histories for halos of masses $M_{\mathrm{halo}} \sim 10^{12.5} M_\odot$ at $z = 2$. The simulation of these galaxies is described in detail by Anglés-Alcázar et al. (2017), but we briefly summarise their methods here. Anglés-Alcázar et al. (2017) build on the sample of massive galaxies at high redshift originally simulated as part of the MassiveFIRE project (Feldmann et al. 2017), adding to this sample a novel implementation of black hole growth. The Anglés-Alcázar et al. (2017) simulations make use of the FIRE-2 code (Hopkins et al. 2017), which improves on the original FIRE-1 code, primarily thanks to improved numerical accuracy. FIRE-2 implements a new, more accurate hydrodynamics solver (a mesh-free Godunov solver; Gaburov & Nitadori 2011; Hopkins 2015), an improved treatment of cooling and recombination rates, gravitational softening and numerical feedback coupling. The new simulations from Anglés-Alcázar et al. (2017) implement baryonic particle masses of $3.3 \times 10^4 M_\odot$, with a minimum softening length for the gas of 0.7pc.

Our sample of FIRE-2 galaxies represent the most realistic, massive, high redshift galaxies ever simulated at high resolution. This enables us to study the types of galaxies that might be observed as sub-mm bright by facilities such as ALMA. In Section 2.2, we present the four

galaxies, and the evolution of their modelled properties with redshift.

2.2 Selection of sub-mm-bright galaxy snapshots at $z > 2$

We wish to study galaxies within the FIRE-2 simulation at snapshots for which the rest-frame FIR flux is bright, since only sub-mm-bright galaxies are typically observed with ALMA at high redshifts. Performing radiative transfer on each of the 600 redshift snapshots to predict sub-mm fluxes and then selecting the brightest would be impossibly computationally intensive. The first step in our analysis is therefore to select redshift snapshots for each of the four galaxies in which we expect the sub-mm flux to be particularly bright, using simply the SFR and dust mass at each snapshot (see Figure 1). We adopt the following equation, derived from fits to the sub-mm flux densities of simulated galaxies and presented in Hayward et al. (2013):

$$f_{850\mu\mathrm{m}} = 0.81\mathrm{mJy} \times \left(\frac{\mathrm{SFR}}{100\mathrm{M}_{\odot}\mathrm{yr}^{-1}}\right)^{0.43} \left(\frac{\mathrm{M_{dust}}}{10^{8}\mathrm{M}_{\odot}}\right)^{0.54} \quad (1)$$

Initially, we use a crude assumption that $M_{\mathrm{dust}} = 0.01 M_{\mathrm{gas}}$, as the dust mass is not available at every snapshot for each galaxy. This simple formula results in an overestimation of the dust mass, and hence the 850μm flux, but this is not critical for the snapshot selection. We select those snapshots with highest predicted $f_{850\mu\mathrm{m}}$ from each simulated galaxy (named A1, A2, A4 & A8). We do not attempt to produce a complete sample of sub-mm bright galaxies within the FIRE-2 simulations; instead, our selection is sufficient to yield a small sample of sub-mm bright snapshots for which we can perform radiative transfer and study multi-wavelength properties.

3 RADIATIVE TRANSFER METHODS AND RESULTS

3.1 Performing radiative transfer with SKIRT

Modelling dust and its emission in galaxies is a difficult computational problem (see Steinacker et al. 2013, for a comprehensive review). The process of radiative transfer is non-local in space (photons can propagate long distances before interacting with dust), and it is coupled in terms of both direction and wavelength. The distribution of dust in galaxies is far from a simple screen, instead requiring a full 3-dimensional model of the radiative transfer between matter and radiation. The geometries of stars and dust particles are resolved on a 3-dimensional grid on which the radiative transfer is performed. A well-resolved grid is particularly important where the dust distribution is clumpy, as it sometimes appears in high redshift galaxies.

In this work, we make use of the Stellar Kinematics Including Radiative Transfer (SKIRT) Monte Carlo radiative transfer code (Baes et al. 2011; Camps & Baes 2014). Monte Carlo radiative transfer codes like SKIRT treat the radiation field from stars as a flow of photons through the dusty medium of a galaxy. The simulation is updated at every time step, as photons are emitted, scattered, and absorbed by dust. This iteration allows the code to take into account the emission of photons from dust particles self-consistently. Unlike general ray-tracing approaches to radiative transfer, in Monte Carlo codes, the emission, scattering and absorption processes are each governed by random numbers drawn from probability distributions at every timestep.

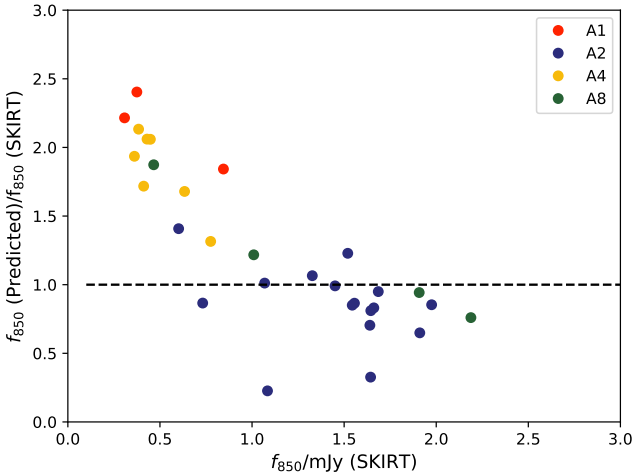

Figure 2: Predicted 850μm flux (from the models of Hayward et al. 2013) divided by SKIRT-output flux, as a function of SKIRT-output flux. The agreement is very good for fluxes above $\sim$ 1mJy.

We extract gas and star particles from the FIRE-2 simulations for each time snapshot at which we perform the radiative transfer. All particles are rotated to align with the angular momentum vector of the gas particles prior to input to SKIRT, so that a viewing angle of 0 degrees corresponds to a face-on galaxy. We generate dust particle positions from the gas particles, applying a temperature cut of 10^6K (on the assumption that dust particles will be destroyed at temperatures higher than this). We derive dust particle masses using the metallicity of the gas particles and a dust-to-metals mass ratio of 0.4. We use a Weingartner & Draine (2001) Milky Way dust prescription to model a mixture of graphite, silicate and PAH grains. Star particles were assigned a *Starburst99* spectral energy distribution (Leitherer et al. 1999). We use an octree dust grid, in which cell sizes are adjusted according to the dust density distribution. We impose the condition that no dust cell may contain more than 0.0001% of the total dust mass of the galaxy, which gives excellent convergence.

We also specify a number of properties relating to the SED output. We define a wavelength grid with $\sim$ 100 discrete wavelengths, spaced between rest-frame UV and FIR wavelengths. To model the flux that would be received by an observer on Earth, we place seven detectors at $z = 0$, arranged at uniform inclinations with respect to the galaxy. These detectors have pixel sizes corresponding to a proper length of 25pc out to $0.1R_{\mathrm{virial}}$ for each galaxy snapshot studied.

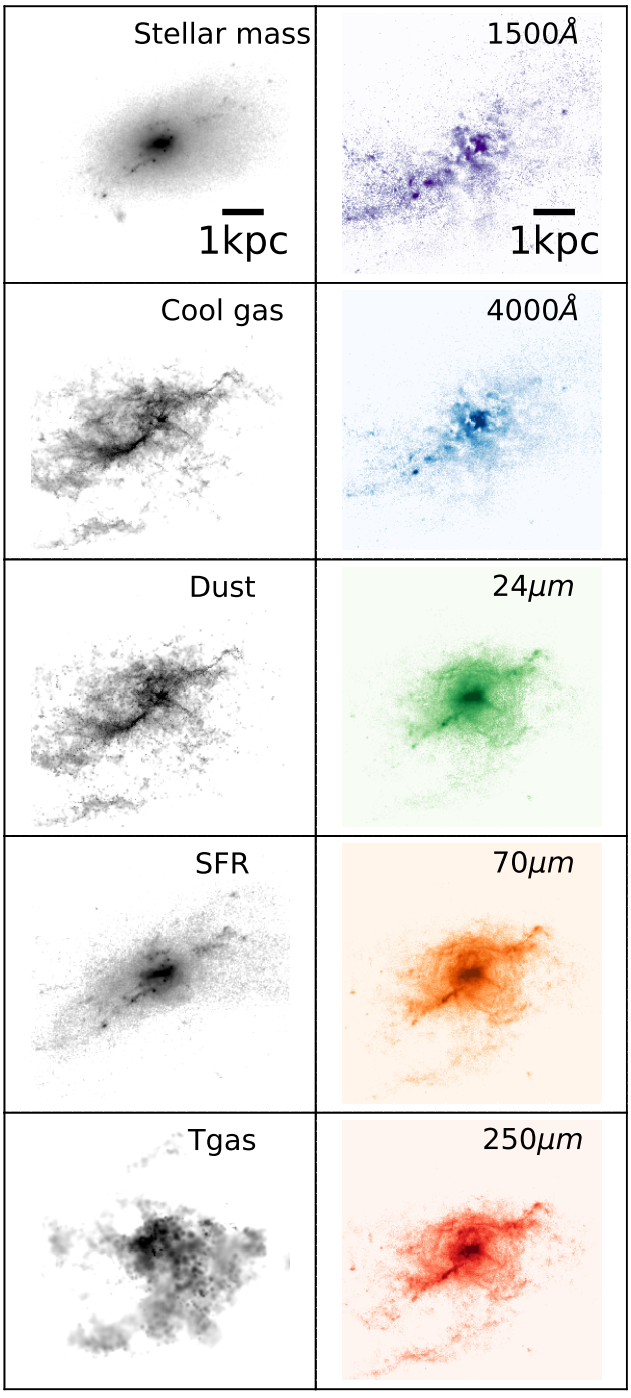

Figure 3: The wavelength-dependent morphology of galaxy A1 at z=4.38. The left hand panel shows the intrinsic properties of the galaxy. The right hand panel shows the SKIRT-predicted spatial distribution of emission at different rest-frame wavelengths. The morphology is strongly dependent on the wavelength. The galaxy appears clumpy and extended in the rest-frame UV, and more ordered at longer wavelengths. Colourbars are not shown as we explore only the qualitative differences in morphology. However, all panels span the same range (70-99% of maximum flux).

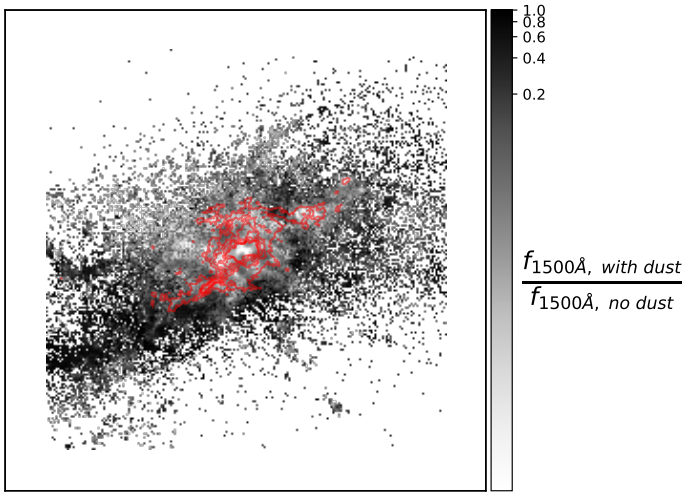

Figure 4: The ratio of rest-frame 1500Å light predicted after full radiative transfer including dust, to that predicted in simulations without dust, for galaxy A1 at $z = 4.38$. Contours of the rest-frame $250\mu m$ emission are overlaid in red. The long- and short-wavelength emission are spatially anti-correlated: where dust emission is greatest, less FUV light escapes the galaxy.

3.2 SKIRT-output $850\mu m$ flux compared to predictions

As described in Section 3.1, we model dust particles within each FIRE-2 galaxy snapshot using a dust-to-metals mass ratio of 0.4 and assuming that dust traces gas at temperatures $< 10^6$K. Inputting these dust masses directly into Equation 1 enables us to refine our predictions for the observed-frame $850\mu m$ flux for the subset of galaxy snapshots selected in Section 2.2. Our predicted fluxes span the range 0.3 – 3mJy. The agreement between these predictions and the $850\mu m$ fluxes output by SKIRT are presented in Figure 2. The agreement for fluxes above ~ 1mJy is encouraging.

3.3 Morphology across the wavelength spectrum

We derive images of each of the galaxy snapshots at ~ 100 wavelengths from the rest-frame far-UV to rest-frame far-IR. We find that the same galaxy looks vastly different in the different wavebands. We illustrate this qualitatively with five representative wavelengths for galaxy A1 at $z = 4.38$ in Figure 3 and galaxy A2 at $z = 2.95$ in Figure 5. We also show the spatial distributions of five key galaxy properties: total stellar mass, cool ($T < 10^6$K) gas mass, dust mass, recently formed stars (age < 100Myr), and gas temperature.

Galaxy A1 at snapshot $z = 4.38$ has a SKIRT-predicted observed-frame $850\mu m$ flux of 0.84mJy. At this snapshot, the galaxy displays very clumpy FUV emission (rest-frame 1500Å), spanning a few kpc. This emission is oriented along the axis of the gas, and displays peaks where the gas is densest. The optical emission (rest-frame 4000Å) is also clumpy. Longwards of $24\mu m$, the emission becomes significantly more centrally concentrated, resembling the total and recently formed stellar mass distribution more closely. The long- and

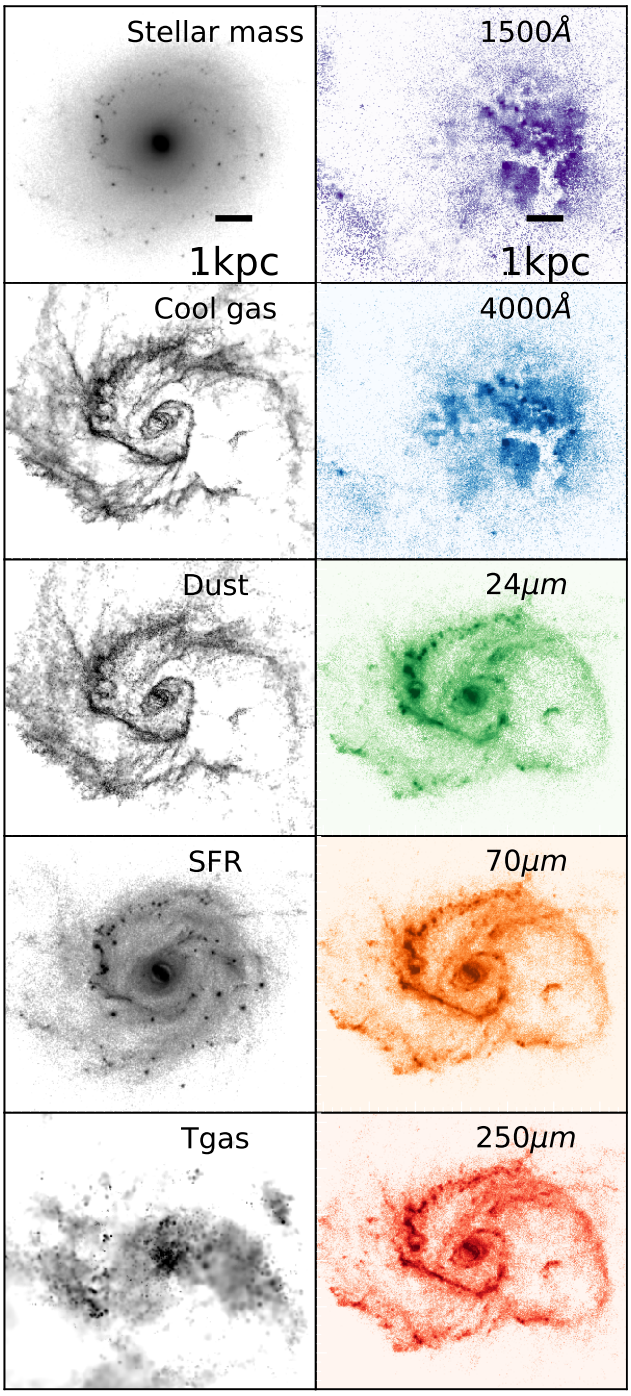

Figure 5: The wavelength-dependent morphology of galaxy A2 at z=2.95. The UV and optical light is significantly offset from peak of the stellar mass and SFR, appearing to trace holes in the dust distribution.

short-wavelength emission are spatially anti-correlated, as shown by Figure 4. It appears that the clumpy FUV emission is driven by the structure of the dust component, with FUV emission tracing holes in the dust.

Galaxy A2 at snapshot $z = 2.95$ is brighter, with a SKIRT-predicted observed-frame 850μm flux of 1.54mJy. It

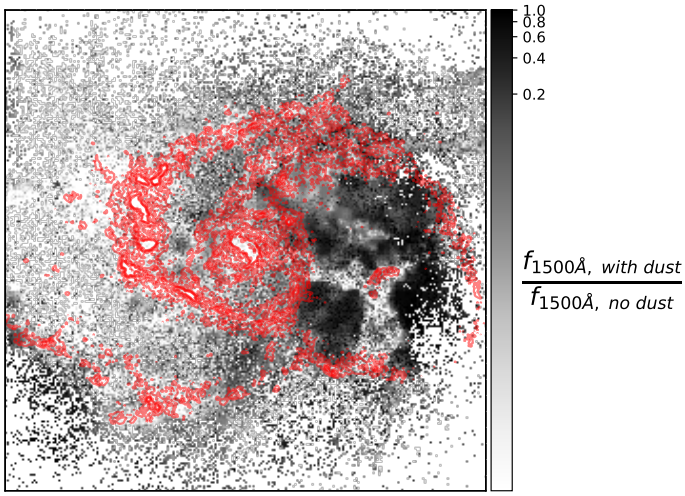

Figure 6: The ratio of rest-frame 1500Å light predicted after full radiative transfer including dust, to that predicted in simulations without dust, for galaxy A2 at z=2.95. Contours of the rest-frame 250μm emission are overlaid in red. The rest-frame FUV and FIR emission predicted after radiative transfer with dust occupy strikingly different spatial regions. While there is recent star formation across the extent of the galaxy disk, light at short wavelengths does not escape from regions of high dust density. Therefore, FUV emission is spatially offset from long wavelength emission.

is also substantially more extended in all wavebands. The rest-frame 1500Å and 4000Å emission is again clumpy, bearing little resemblance to the ordered bulge + spiral structure that is clear from the stellar mass, gas/dust mass and SFR maps. The short-wavelength emission occupies a region to the right of centre that is largely free of dust (see Figure 6). Future work will explore the resolved multi-wavelength emission on a pixel-by-pixel basis.

4 QUANTIFYING THE SPATIAL EXTENT OF DUST CONTINUUM EMISSION

4.1 The dependence of size on FIR wavelength

In this section we attempt to quantify the sizes of sub-mm-bright FIRE-2 galaxies as a function of wavelength. An example of the observed-frame SED predicted by SKIRT, overplotted with the wavelengths corresponding to eight ALMA bands, is shown in Figure 7 (left-hand panel). We extract the SKIRT image at each of these wavelengths and derive an 'effective radius' for the predicted emission. This is defined here as the half-light radius derived using a circular aperture centered on the flux-weighted center defined by the emission in each band. In each case, an error bar is derived from the standard deviation of the effective radius measurements at different galaxy/detector inclinations.

In the right-hand panel of Figure 7, we show an example of our results. The effective radius of the emission varies significantly with wavelength (in this example, by roughly a factor of two), with longer wavelength FIR emission span-

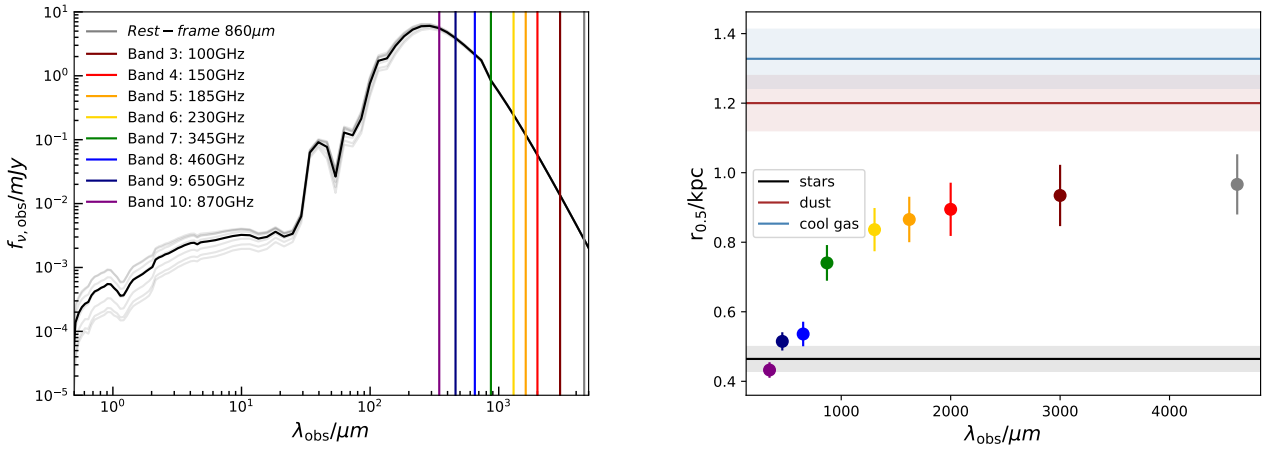

Figure 7: Left: observed-frame SKIRT-output SED for galaxy A1, at $z = 4.38$, with ALMA bands overlaid. Right: the effective radii of the emission at the wavelengths of each of these bands, compared to those of the galaxy stellar mass, cold gas mass and dust mass. Shorter wavelength FIR emission better traces the stellar component, whereas longer wavelength emission traces the cold gas and dust.

ning a greater spatial extent. We also overplot the effective radii of several key physical quantities of the galaxy: stellar mass, dust mass and cool gas mass ($T < 10^6$K). In this example and in general, the cool gas mass extends to larger radii than the dust mass, with stellar mass being most compact. The sizes of the dust continuum emission tend to be between those of the dust mass and the stellar mass. Shorter wavelength FIR emission better traces the stellar component, whereas longer wavelength FIR emission traces the cold gas and dust.

The 870μm (345GHz) observed-frame emission, probed by ALMA Band 7 is frequently used to study the dust continuum emission of high redshift galaxies (e.g. Barro et al. 2016; Chen et al. 2017; Simpson et al. 2017). Our derived 870μm effective radii are $\sim 0.5 - 3$kpc. This is in excellent agreement with observations at a range of redshifts (e.g. Ikarashi et al. 2015; Iono et al. 2016; Simpson et al. 2015; Hodge et al. 2016). For simplicity, from here on we consider only the 870μm flux in our discussion of the spatial extent of the dust continuum emission. However, we note that we consistently find that emission at longer rest-frame FIR wavelengths is more extended, as shown in Figure 7.

4.2 How does the dust continuum emission trace the physical properties of galaxies?

The dust continuum emission is frequently used as an indicator of both star-formation rate and dust mass. However, until now the spatial extent of these physical and observable quantities has not been studied consistently with simulated galaxies. Motivated by the clear differences in effective radii of the dust continuum emission, stellar mass, dust mass, and gas mass found for individual FIRE-2 galaxies (see Figure 7), we set out to identify which physical properties are best reflected by the spatial extent of the dust continuum emission.

In Figure 8 we show the effective radii of the 870μm dust emission versus that of the cool gas. All snapshots of each of the four FIRE-2 galaxies lie below the 1-1 line (dashed black); dust emission is more compact than the cool gas in all cases. This is consistent with existing observations of high redshift galaxies. Both Tadaki et al. (2017) and Calistro Rivera et al. (2018) find that the effective radii of the 870μm emission of galaxies at $z \sim 2.5$ are approximately half those of the cool gas, probed by 12CO(J = 3 – 2). Although our analysis does not consider the different temperature regions probed by different CO lines in detail, our predictions are in good agreement with the small number of high redshift galaxies that have been observed in both dust continuum and CO at high spatial resolution.

We also consider how the spatial extent of dust emission correlates with that of the total and recently-formed stellar mass. We find that, in general, the emission from dust is more extended than both (see Figure 9). The extent of recently formed stars appears to correlate more tightly with the extent of the dust emission than the total stellar mass does. This makes sense, as we expect that it is primarily the young stars that act as a heating source for the dust grains that reprocess their short-wavelength light.

In Figure 10 we show the effective radius of 870μm emission versus that of the dust mass itself. Like the cold gas, the dust is more extended than the continuum emission, although the two are clearly well-correlated. Colour-coding the snapshots by the effective radius of the recently formed stellar mass reveals that those galaxies with extremely compact star formation also have extremely compact 870μm emission. This reflects the dual role of the dust mass and star-formation rate in determining the spatial extent of the dust continuum emission.

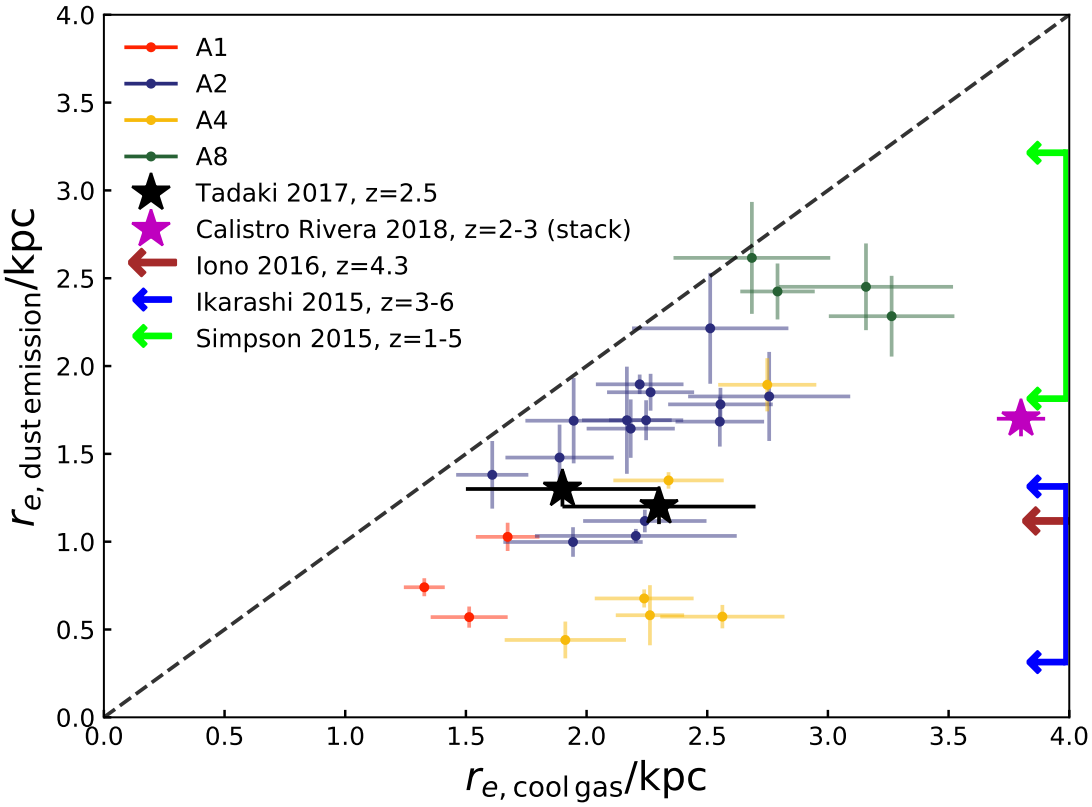

Figure 8: The effective radii of the 870μm dust emission versus that of the cool gas. The dashed black line shows the 1-1 relation. For all galaxies, the dust emission is more compact than the cool gas at all redshift snapshots studied. Overplotted are the following ALMA observations of galaxies at similar redshifts: 870μm emission and 12CO(J = 3 – 2) line flux for two massive ($M_* \sim 10^{11} M_\odot$) galaxies at $z = 2.5$, from Tadaki et al. 2017 (black stars); the effective radii for stacked ALMA maps of 870μm and 12CO(J = 3 – 2) emission for 16 ALESS galaxies at $z = 2.5 \pm 0.2$, from Calistro Rivera et al. 2018 (purple star). We also plot data from sources with only ALMA dust continuum emission as arrows on the y-axis. These include: the 860μm emission from AZTEC-1, a $z = 4.34$ galaxy studied by Iono et al. 2016 (brown arrow); the 1100μm emission for 13 AzTEC galaxies at $z = 3 - 6$, from Ikarashi et al. 2015 (blue); 870μm emission of 23 sub-mm galaxies in the UDS field at $z = 1 - 5$, from Simpson et al. 2015 (green). Although observed sample sizes are small, agreement with our predictions is extremely good.

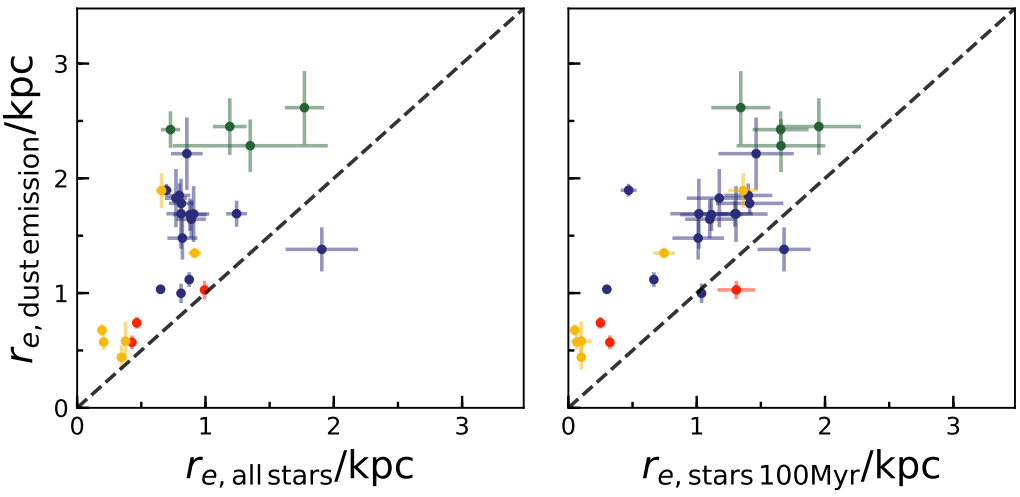

Figure 9: The effective radii of the 870μm dust emission versus that of all stellar mass (left) and stellar mass formed within the last 100Myr (right). The stellar mass tends to be more compact than the dust continuum emission.

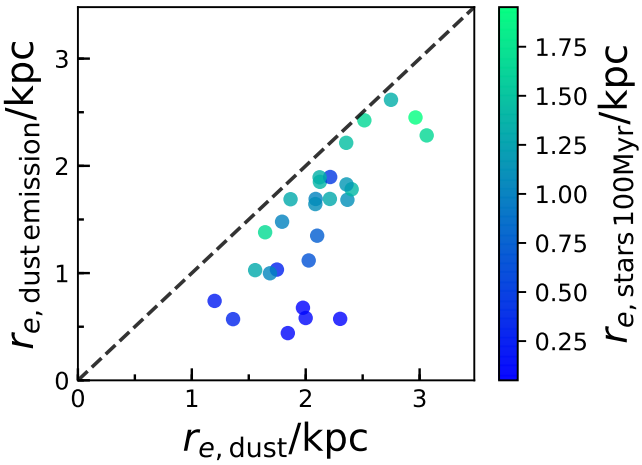

Figure 10: Effective radius of observed-frame dust emission, versus effective radius of dust mass, colour-coded by the effective radius of recently-formed stars. The dust emission is well-correlated with the dust mass spatially, though it tends to be more compact. Very compact regions of recent star-formation appear to be associated with the most compact dust emission.

4.3 Does the extent of dust mass or SFR correlate better with dust continuum emission?

Principal Component Analysis (PCA) is a statistical technique used to describe the variance within a dataset. Variables are converted into a set of uncorrelated, orthogonal principal components. The first component reveals the direction of maximum variance, which describes the key correlation between variables within the dataset. Successive components contain less of the variance of the population. Some latter components may be dominated by noise, leaving the data decomposed into fewer dimensions. PCA has been used in a number of recent galaxy evolution studies, including in studies of the mass-metallicity relation (Lagos et al. 2016; Bothwell et al. 2016; Hashimoto et al. 2018) and to study the quenching of galaxies within the EAGLE simulations (Cochrane & Best 2018).

Here, we use PCA to study the relationship between effective radii of dust mass, SFR and dust continuum emission. We use the PCA python tool *scikit.learn* to perform the PCA analysis. Each variable is normalized to its mean and scaled to unit variance before input to the PCA. For each snapshot studied, we construct a vector of the form [$r_{\mathrm{eff,\ dust\ emission}}$, $r_{\mathrm{eff,\ dust\ mass}}$, $r_{\mathrm{eff,\ young\ stars}}$], and supply all these vectors to the PCA.

We find that the first principal component, [0.71, 0.38, 0.59], almost entirely describes the dataset, containing 83% of the variance of the sample. This indicates that all three variables - the effective radii of dust emission, dust mass and recently formed stars, are positively correlated. The effective radius of the dust emission is more strongly correlated with the effective radius of the recently formed stars than with the effective radius of the dust mass itself, according to their magnitudes. The second principal component, [-0.13, -0.76, 0.64], contains almost all of the rest of the variance of the sample, 13%. This encapsulates the scatter in the relationship between the effective radii of the dust mass and the recently formed stars.

From this analysis, it appears that the extent of the dust continuum emission is slightly better correlated with the extent of the recently formed stars, than with that of the dust mass distribution itself. The second principal component has essentially zero variance; this means that the extent of the dust continuum emission can essentially be defined by the other two parameters - the extent of the dust and recently formed stars, with the later being the more critical.

5 CONCLUSIONS

We have performed radiative transfer modelling on a subset of rest-frame FIR-bright redshift snapshots of four galaxies drawn from the FIRE-2 simulations. This modelling yields full rest-frame FUV-FIR SEDs as well as maps of the emission in $\sim$ 100 wavebands, resolved to 25pc scales. We find clear differences between the morphologies of the same galaxies in the different wavebands, with shorter-wavelength emission (UV/optical) appearing clumpy and extended. We find that this is due to the emitted short-wavelength light tracing 'holes' in the dust distribution. At rest-frame FIR wavelengths, the galaxies tend to have more regular morphologies.

The primary focus of our study is the spatial extent of the dust continuum emission. At the snapshots we study, FIRE-2 galaxies have observed-frame 870μm fluxes of up to $\sim$ 2mJy at $z \sim 2-5$. These simulated FIR-bright galaxies display very compact dust continuum emission of $\sim 0.5-3$kpc, in line with existing observations of star-forming galaxies at these redshifts. At rest-frame FIR wavelengths (which we can probe with ALMA for high redshift galaxies), slightly longer wavelength light tends to span the largest spatial extent.

We also compare the spatial extent of the 870μm dust continuum emission to that of a few key intrinsic physical quantities: the dust mass, gas mass and star-formation rate. In both simulated and observed galaxies, the dust continuum emission is more compact than the cold gas and the dust, but more extended than the stellar component. Extracting only recently formed (age < 100Myr) stars from the simulations enables us to study the role of recent star formation in determining the spatial extent of the dust emission. We find that at some snapshots, the simulated galaxies display extremely compact dust emission ($\sim$ 0.5kpc). This emission appears to be driven by particularly compact recent star formation. Overall, the spatial extent of the dust continuum emission correlates with that of both the dust mass and the recently formed stars. Physically, this makes sense: the dust that emits strongly in the FIR is heated by star-formation, and where this star formation is particularly compact, the central regions of dust are preferentially heated.

6 WORK PLANNED BEYOND THE KAVLI SUMMER PROGRAM

- **A study of the offsets between emission in different wavebands.**
  We show in Figures 4 & 6 that emission at long wavelengths can be substantially spatially offset from short-wavelength emission and from CO line emission. This is consistent with current observations of high-redshift galaxies (e.g. Hodge et al. 2015, 2016; Simpson et al. 2017, Cochrane et al. in prep.). In future work, we aim to measure the flux-weighted centres of simulated FIRE-2 galaxies at different wavelengths spanning the full FUV-FIR range. We will then explore how the magnitudes of these offsets depend on the underlying properties of the galaxy, such as dust mass, and compare our results to observations.

- **Spatially-resolved galaxy scaling relations**
  Simulating the emission from FIRE-2 galaxies on pixel scales of 25pc means that we can correlate the pixel-scale emission in different wavelengths to the pixel-scale physical properties of the galaxy. This will enable us to study spatially-resolved scaling relations such as $f_{850\mu m}$-SFR, $f_{850\mu m}$-$M_{\rm dust}$ and $f_{850\mu m}$-$M_{\rm gas}$ to arbitrarily high spatial resolution. Grouping pixels in different ways (e.g. 2x2 pixels versus 10x10 pixels) will permit a study of the minimum scales to which scaling relations derived from spatially-unresolved measurements hold.

- **Predictions for extremely high spatial resolution ALMA observations**
  Some recent ALMA observations of dusty star-forming galaxies at $z > 2$ suggest that their star-forming regions are compact and clumpy, while others are consistent with smooth, compact disks. It remains unclear whether observed 'clumps' are intrinsic features of high redshift galaxies, or observational artefacts arising from the instrument's sensitivity limit (see Gullberg et al. 2018). We hope to use the predictions of the dust continuum emission from FIRE-2 galaxies, in combination with ALMA simulator tools, to study how the apparent clumpiness of high redshift observed galaxies depends on the resolution and sensitivity of observations.

ACKNOWLEDGEMENTS

This work was initiated as a project for the Kavli Summer Program in Astrophysics held at the Center for Computational Astrophysics of the Flatiron Institute in 2018. The program was co-funded by the Kavli Foundation and the Simons Foundation. We thank them for their generous support.

REFERENCES

Anglés-Alcázar D., Faucher-Giguère C. A., Quataert E., Hopkins P. F., Feldmann R., Torrey P., Wetzel A., Kereš D., 2017, MNRAS Lett., 472, L109
Baes M., Verstappen J., De Looze I., Fritz J., Saftly W., Vidal Pérez E., Stalevski M., Valcke S., 2011, ApJSS, 196
Barro G., et al., 2016, ApJL, 827, 1
Beckwith S., Stiavelli M., Koekemoer A. M., Caldwell J. A. R., Ferguson H. C., Hook R., 2006, ApJ, 132, 1729
Behroozi P. S., Wechsler R. H., Conroy C., 2013, ApJ, 770, 57
Bothwell M. S., Maiolino R., Cicone C., Peng Y., Wagg J., 2016, A&A, p. A48
Bouwens R. J., et al., 2010, ApJL, 709, 133
Bowler R. A. A., Bourne N., Dunlop J. S., Mclure R. J., Mcleod D. J., 2018, MNRAS
Calistro Rivera G., et al., 2018, Astrophys. J., 863, 56
Camps P., Baes M., 2014,] 10.1016/j.ascom.2014.10.004
Chen C.-C., et al., 2017, ApJ, 846, 108
Cochrane R. K., Best P. N., 2018, MNRAS, 480, 864
Dale J. E., 2015, New Astron. Rev., 68, 1
Dekel A., et al., 2009, Nature, 457, 451
Dunlop J. S., et al., 2013, MNRAS, 432, 3520
Dunlop J. S., et al., 2017, MNRAS, 466, 861
Ellis R. S., et al., 2013, ApJL, 763, 8
Elmegreen B. G., Elmegreen D. M., Sánchez Almeida J., Muñoz-Tuñón C., Dewberry J., Putko J., Teich Y., Popinchalk M., 2013, ApJ, 774
Feldmann R., Quataert E., Hopkins P. F., Faucher-Giguére C. A., Kereš D., 2017, MNRAS, 470, 1050
Gaburov E., Nitadori K., 2011, MNRAS, 414, 129
Genzel R., et al., 2008, ApJ, 687, 59
Gullberg B., et al., 2018, ApJ, 859, 12
Guo Y., et al., 2015, ApJ, 800, 39
Hashimoto T., Goto T., Momose R., 2018, arXiv eprint:1801.05808
Hayward C. C., Kere D., Jonsson P., Narayanan D., Cox T. J., Hernquist L., 2011, ApJ, 743
Hayward C. C., Narayanan D., Kereš D., Jonsson P., Hopkins P. F., Cox T. J., Hernquist L., 2013, MNRAS, 428, 2529
Hodge J. A., Riechers D., Decarli R., Walter F., Carilli C. L., Daddi E., Dannerbauer H., 2015, Astrophys. J. Lett., 798, 1
Hodge J. A., et al., 2016, ApJ, 833, 1
Hopkins P. F., 2015, MNRAS, 450, 53
Hopkins P. F., Quataert E., Murray N., 2011, MNRAS, 417, 950
Hopkins P. F., Kereš D., Oñorbe J., Faucher-Giguère C. A., Quataert E., Murray N., Bullock J. S., 2014, MNRAS, 445, 581
Hopkins P. F., et al., 2017, 000
Ikarashi S., et al., 2015, Astrophys. J., 810, 133
Ilbert O., et al., 2013, A&A, 55, 1
Illingworth G. D., et al., 2013, ApJSS, 209
Iono D., et al., 2016, ApJL, 829, 1
Kennicutt R. C., 1998, ApJ, 498, 541
Kennicutt R. C., Evans N. J., 2012, A&A Rev., 50, 531
Lagos C. D. P., et al., 2016, MNRAS, 459, 2632
Leitherer C., et al., 1999, ApJSS, 123, 3
Ma X., Hopkins P. F., Faucher-Giguère C. A., Zolman N., Muratov A. L., Kereš D., Quataert E., 2016, MNRAS, 456, 2140
Moster B. P., Somerville R. S., Maulbetsch C., Bosch F. C. V. D., Macci A. V., Naab T., Oser L., 2010, ApJ, 710, 903
Muzzin A., Marchesini D., Stefanon M., Franx M., Mccracken H. J., Milvang-jensen B., Dokkum P. G. V., 2013, ApJ, p. 18
Oesch P. A., et al., 2010, ApJL, 709
Oliver S. J., et al., 2012, Mon. Not. R. Astron. Soc., 424, 1614
Scudder J. M., Oliver S., Hurley P. D., Griffin M., Sargent M. T., Scott D., Wang L., Wardlow J. L., 2016, Mon. Not. R. Astron. Soc., 460, 1119
Simpson J. M., et al., 2015, Astrophys. J., 799, 81
Simpson J. M., et al., 2017, ApJL, 844, 6
Sparre M., Hayward C. C., Feldmann R., Faucher-Giguère C. A., Muratov A. L., Kereš D., Hopkins P. F., 2017, MNRAS, 466, 88
Steinacker J., Baes M., Gordon K., 2013, ARAA, pp 63–105
Tacconi L. J., Genzel R., Neri R., Cox P., Cooper M. C., Shapiro K., Bolatto A., 2010, Nature, 463, 781

Tacconi L. J., et al., 2013, ApJ, 768, 74
Tadaki K.-i., et al., 2017, ApJL, 841, L25
Weingartner J. C., Draine B. T., 2001, ApJ, 548, 296
van de Voort F., Quataert E., Hopkins P. F., Kereš D., Faucher-Giguére C. A., 2015, MNRAS, 447, 140